

# Very-high-energy particle acceleration powered by the jets of the microquasar SS 433

A. U. Abeysekara<sup>1</sup>, A. Albert<sup>2</sup>, R. Alfaro<sup>3</sup>, C. Alvarez<sup>4</sup>, J. D. Álvarez<sup>5</sup>, R. Arceo<sup>4</sup>, J. C. Arteaga-Velázquez<sup>5</sup>, D. Avila Rojas<sup>3</sup>, H. A. Ayala Solares<sup>6</sup>, E. Belmont-Moreno<sup>3</sup>, S. Y. BenZvi<sup>7,35</sup>, C. Brisbois<sup>8</sup>, K. S. Caballero-Mora<sup>4</sup>, T. Capistrán<sup>9</sup>, A. Carramiñana<sup>9</sup>, S. Casanova<sup>10</sup>, M. Castillo<sup>5</sup>, U. Cotti<sup>5</sup>, J. Cotzomi<sup>11</sup>, S. Coutiño de León<sup>9</sup>, C. De León<sup>12</sup>, E. De la Fuente<sup>12</sup>, J. C. Díaz-Vélez<sup>13,14</sup>, S. Dichiara<sup>13</sup>, B. L. Dingus<sup>2,35</sup>, M. A. DuVernois<sup>14</sup>, R. W. Ellsworth<sup>15</sup>, K. Engel<sup>16</sup>, C. Espinoza<sup>3</sup>, K. Fang<sup>17,18,35</sup>, H. Fleischhacker<sup>8</sup>, N. Fraija<sup>13</sup>, A. Galván-Gámez<sup>13</sup>, J. A. García-González<sup>3</sup>, F. Garfias<sup>13</sup>, A. González-Muñoz<sup>3</sup>, M. M. González<sup>13</sup>, J. A. Goodman<sup>16</sup>, Z. Hampel-Arias<sup>14,19</sup>, J. P. Harding<sup>2</sup>, S. Hernandez<sup>3</sup>, J. Hinton<sup>20</sup>, B. Hona<sup>8</sup>, F. Hueyotl-Zahuantitla<sup>4</sup>, C. M. Hui<sup>21</sup>, P. Hüntemeyer<sup>8</sup>, A. Iriarte<sup>13</sup>, A. Jardin-Blicq<sup>20</sup>, V. Joshi<sup>20</sup>, S. Kaufmann<sup>4</sup>, P. Kar<sup>1</sup>, G. J. Kunde<sup>2</sup>, R. J. Lauer<sup>22</sup>, W. H. Lee<sup>13</sup>, H. León Vargas<sup>3</sup>, H. Li<sup>2</sup>, J. T. Linnemann<sup>22</sup>, A. L. Longinotti<sup>9</sup>, G. Luis-Raya<sup>23</sup>, R. López-Coto<sup>24</sup>, K. Malone<sup>6</sup>, S. S. Marinelli<sup>22</sup>, O. Martinez<sup>11</sup>, I. Martinez-Castellanos<sup>16</sup>, J. Martínez-Castro<sup>25</sup>, J. A. Matthews<sup>26</sup>, P. Miranda-Romagnoli<sup>27</sup>, E. Moreno<sup>11</sup>, M. Mostafá<sup>6</sup>, A. Nayerhoda<sup>10</sup>, L. Nellen<sup>28</sup>, M. Newbold<sup>1</sup>, M. U. Nisa<sup>7</sup>, R. Noriega-Papaqui<sup>27</sup>, J. Pretz<sup>6</sup>, E. G. Pérez-Pérez<sup>23</sup>, Z. Ren<sup>26</sup>, C. D. Rho<sup>7,35\*</sup>, C. Rivière<sup>16</sup>, D. Rosa-González<sup>9</sup>, M. Rosenberg<sup>6</sup>, E. Ruiz-Velasco<sup>20</sup>, F. Salesa Greus<sup>10</sup>, A. Sandoval<sup>3</sup>, M. Schneider<sup>29</sup>, H. Schoorlemmer<sup>20</sup>, M. Seglar Arroyo<sup>6</sup>, G. Sinnis<sup>2</sup>, A. J. Smith<sup>16</sup>, R. W. Springer<sup>1</sup>, P. Surajbali<sup>20</sup>, I. Taboada<sup>30</sup>, O. Tibolla<sup>4</sup>, K. Tollefson<sup>22</sup>, I. Torres<sup>9</sup>, G. Vianello<sup>31</sup>, L. Villaseñor<sup>11</sup>, T. Weisgarber<sup>14</sup>, F. Werner<sup>20</sup>, S. Westerhoff<sup>14</sup>, J. Wood<sup>14</sup>, T. Yapici<sup>7</sup>, G. Yodh<sup>32</sup>, A. Zepeda<sup>33</sup>, H. Zhang<sup>34,35</sup> & H. Zhou<sup>2,35\*</sup>

**SS 433 is a binary system containing a supergiant star that is overflowing its Roche lobe with matter accreting onto a compact object (either a black hole or neutron star)<sup>1–3</sup>. Two jets of ionized matter with a bulk velocity of approximately 0.26c (where c is the speed of light in vacuum) extend from the binary, perpendicular to the line of sight, and terminate inside W50, a supernova remnant that is being distorted by the jets<sup>2,4–8</sup>. SS 433 differs from other microquasars (small-scale versions of quasars that are present within our own Galaxy) in that the accretion is believed to be super-Eddington<sup>9–11</sup>, and the luminosity of the system is about  $10^{40}$  ergs per second<sup>2,9,12,13</sup>. The lobes of W50 in which the jets terminate, about 40 parsecs from the central source, are expected to accelerate charged particles, and indeed radio and X-ray emission consistent with electron synchrotron emission in a magnetic field have been observed<sup>14–16</sup>. At higher energies (greater than 100 gigaelectronvolts), the particle fluxes of  $\gamma$ -rays from X-ray hotspots around SS 433 have been reported as flux upper limits<sup>6,17–20</sup>. In this energy regime, it has been unclear whether the emission is dominated by electrons that are interacting with photons from the cosmic microwave background through inverse-Compton scattering or by protons that are interacting with the ambient gas. Here we report teraelectronvolt  $\gamma$ -ray observations of the SS 433/W50 system that spatially resolve the lobes. The teraelectronvolt emission is localized to structures in the lobes, far from the centre of the system where the jets are formed. We have measured photon energies of at least 25 teraelectronvolts, and these are certainly not**

Doppler-boosted, because of the viewing geometry. We conclude that the emission—from radio to teraelectronvolt energies—is consistent with a single population of electrons with energies extending to at least hundreds of teraelectronvolts in a magnetic field of about 16 microgauss.

In the SS 433/W50 complex, several regions located west of the central binary (w1 and w2) and east (e1, e2, e3) are observed to emit hard X-rays<sup>6</sup>. Previous searches for very high-energy (VHE)  $\gamma$ -ray emission from the hotspots between roughly 100 GeV and 10 TeV have produced null results<sup>17–20</sup>, though an excess observed at about 800 MeV may be associated with SS 433 and W50<sup>21</sup>. The High Altitude Water Cherenkov (HAWC) observatory, Mexico, is a wide field-of-view VHE  $\gamma$ -ray observatory surveying the Northern Hemisphere above 1 TeV, and is optimized for photon detection above 10 TeV<sup>22</sup>. SS 433 transits 15° from the zenith of the HAWC detector each day, and has been observed with >90% uptime since the start of detector operations in 2015.

In 1,017 days of measurements with HAWC, an excess of  $\gamma$ -rays with a post-trials significance of  $5.4\sigma$  has been observed in a joint fit of the eastern and western interaction regions of the jets of SS 433. The emission is plotted in galactic coordinates in Fig. 1, which includes an overlay of the X-ray observations of the jets and the central binary. The  $\gamma$ -ray emission is spatially coincident with the X-ray hotspots w1 and e1; no significant emission is observed at the location of the central binary where the jets are produced.

Spatial and spectral fits to SS 433 are performed in a semicircular region of interest (ROI) designed to mask out diffuse emission from

<sup>1</sup>Department of Physics and Astronomy, University of Utah, Salt Lake City, UT, USA. <sup>2</sup>Physics and Theoretical Divisions, Los Alamos National Laboratory, Los Alamos, NM, USA. <sup>3</sup>Instituto de Física, Universidad Nacional Autónoma de México, Mexico City, Mexico. <sup>4</sup>Universidad Autónoma de Chiapas, Tuxtla Gutiérrez, Mexico. <sup>5</sup>Universidad Michoacana de San Nicolás de Hidalgo, Morelia, Mexico. <sup>6</sup>Department of Physics, Pennsylvania State University, University Park, PA, USA. <sup>7</sup>Department of Physics and Astronomy, University of Rochester, Rochester, NY, USA. <sup>8</sup>Department of Physics, Michigan Technological University, Houghton, MI, USA. <sup>9</sup>Instituto Nacional de Astrofísica, Óptica y Electrónica, Puebla, Mexico. <sup>10</sup>Institute of Nuclear Physics Polish Academy of Sciences, IFJ-PAN, Krakow, Poland. <sup>11</sup>Max-Planck Institute for Nuclear Physics, Heidelberg, Germany. <sup>12</sup>Facultad de Ciencias Físico Matemáticas, Benemérita Universidad Autónoma de Puebla, Puebla, Mexico. <sup>13</sup>Departamento de Física, Centro Universitario de Ciencias Exactas e Ingenierías, Universidad de Guadalajara, Guadalajara, Mexico. <sup>14</sup>Department of Physics and Wisconsin IceCube Particle Astrophysics Center, University of Wisconsin-Madison, Madison, WI, USA. <sup>15</sup>Instituto de Astronomía, Universidad Nacional Autónoma de México, Mexico City, Mexico. <sup>16</sup>School of Physics, Astronomy, and Computational Sciences, George Mason University, Fairfax, VA, USA. <sup>17</sup>Department of Physics, University of Maryland, College Park, MD, USA. <sup>18</sup>Department of Astronomy, University of Maryland, College Park, MD, USA. <sup>19</sup>Joint Space-Science Institute, University of Maryland, College Park, MD, USA. <sup>20</sup>Inter-university Institute for High Energies, Université Libre de Bruxelles, Brussels, Belgium. <sup>21</sup>NASA Marshall Space Flight Center, Astrophysics Office, Huntsville, AL, USA. <sup>22</sup>Department of Physics and Astronomy, University of New Mexico, Albuquerque, NM, USA. <sup>23</sup>Department of Physics and Astronomy, Michigan State University, East Lansing, MI, USA. <sup>24</sup>Universidad Politécnica de Pachuca, Pachuca, Mexico. <sup>25</sup>INFN and Università di Padova, Padova, Italy. <sup>26</sup>Centro de Investigación en Computación, Instituto Politécnico Nacional, Mexico City, Mexico. <sup>27</sup>Universidad Autónoma del Estado de Hidalgo, Pachuca, Mexico. <sup>28</sup>Instituto de Ciencias Nucleares, Universidad Nacional Autónoma de Mexico, Mexico City, Mexico. <sup>29</sup>Santa Cruz Institute for Particle Physics, University of California, Santa Cruz, Santa Cruz, CA, USA. <sup>30</sup>School of Physics and Center for Relativistic Astrophysics, Georgia Institute of Technology, Atlanta, GA, USA. <sup>31</sup>Department of Physics, Stanford University, Stanford, CA, USA. <sup>32</sup>Department of Physics and Astronomy, University of California, Irvine, Irvine, CA, USA. <sup>33</sup>Physics Department, Centro de Investigación y de Estudios Avanzados del IPN, Mexico City, Mexico. <sup>34</sup>Department of Physics and Astronomy, Purdue University, West Lafayette, IN, USA. <sup>35</sup>These authors contributed equally: S. Y. BenZvi, B. L. Dingus, K. Fang, C. D. Rho, H. Zhang, H. Zhou. \*e-mail: crho2@ur.rochester.edu; hao@lanl.gov

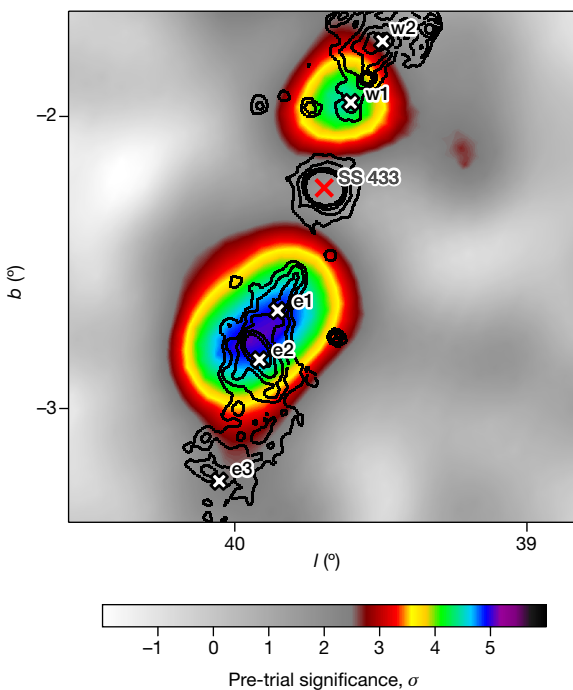


**Fig. 1 | VHE  $\gamma$ -ray image of the SS 433/W50 region in Galactic coordinates.** The colour scale indicates the statistical significance of the excess counts above the background of nearly isotropic cosmic rays before accounting for statistical trials. The figure shows the  $\gamma$ -ray excess measured after the fitting and subtraction of  $\gamma$ -rays from the spatially extended source MGRO J1908+06. The jet termination regions e1, e2, e3, w1 and w2 observed in the X-ray data are indicated, as well as the location of the central binary. The solid contours show the X-ray emission observed from this system.

the Galactic plane. The ROI also removes significant spatially extended emission from the nearby  $\gamma$ -ray source MGRO J1908+06. The spatial distribution and spectrum of  $\gamma$ -rays from MGRO J1908+06 are fitted using an electron diffusion model<sup>23</sup>, and point-like sources centred on e1 and w1 are fitted on top of this extended emission. As a systematic check, the regions are also fitted using X-ray spatial templates and extended Gaussian functions. Neither improves the statistical significance of the fits. Upper limits on the angular size of the emission regions are 0.25° for the east hotspot and 0.35° for the west hotspot at 90% confidence. Given the distance to the source of 5.5 kpc, this corresponds to a physical size of 24 pc and 34 pc, respectively. The constraint is tighter on the eastern hotspot owing to its higher statistical significance.

The VHE  $\gamma$ -ray flux is consistent with a hard  $E^{-2}$  spectrum, though current data from HAWC are not of sufficient significance to constrain the spectral index. Therefore, we report the flux of both hotspots at 20 TeV, at which systematic uncertainties due to the choice of spectral model are minimized and the sensitivity of HAWC is maximized. At e1, the VHE flux is  $2.4^{+0.6}_{-0.5}(\text{stat.})^{+1.3}_{-1.3}(\text{syst.}) \times 10^{-16} \text{ TeV}^{-1} \text{ cm}^{-2} \text{ s}^{-1}$ , and at w1 the flux is  $2.1^{+0.6}_{-0.5}(\text{stat.})^{+1.2}_{-1.2}(\text{syst.}) \times 10^{-16} \text{ TeV}^{-1} \text{ cm}^{-2} \text{ s}^{-1}$ . HAWC detects  $\gamma$ -rays from the interaction regions up to at least 25 TeV. The energies of these  $\gamma$ -rays are a factor of three to ten higher than previous measurements from microquasars<sup>24,25</sup>. Since most  $\gamma$ -ray telescopes are optimized for measurements below 10 TeV, this may explain why these photons were not observed in previous observational campaigns.

The  $\gamma$ -rays detected by HAWC are produced by radiative or decay processes from particles of much higher energy. The detection yields important information about the mechanisms and sites of particle acceleration, the types of particles accelerated (for example, protons or electrons), and the radiative processes that produce the spectrum of emission from radio to VHE  $\gamma$ -rays. Two scenarios for explaining the

HAWC observations of the e1 and w1 regions can be tested. The first is that protons are primarily responsible for the observed  $\gamma$ -rays. Protons must have an energy of at least 250 TeV to produce 25-TeV  $\gamma$ -rays through hadronic collisions with ambient gas. Proton–proton collisions yield neutral pions ( $\pi^0$ ) that decay to VHE  $\gamma$ -rays, and charged pions ( $\pi^\pm$ ) that decay to the secondary electrons and positrons responsible for radio to X-ray emission via synchrotron radiation. This scenario is of particular interest because there is spectroscopic evidence for ionized nuclei in the inner jets of SS 433<sup>8,26</sup>. The alternative scenario requires electrons of at least 130 TeV to up-scatter the low-energy photons from the cosmic microwave background (CMB) to 25-TeV  $\gamma$  rays. In this case, the radio to X-ray emission is dominated by synchrotron radiation from the same population of electrons in the magnetized plasma of the jets and lobes.

The fact that the VHE emission is detected along a line of sight nearly orthogonal to the jet axis means that charged particle trajectories become isotropic before they interact to produce the  $\gamma$ -rays. The embedded magnetic fields in the VHE regions can easily deflect the accelerated particles because their typical gyroradii are much smaller than the size of the emission regions, approximately 30 pc. The jets are only mildly relativistic, so the emission from the interaction regions will have a negligible Doppler beaming effect and remain nearly isotropic.

The flux of VHE  $\gamma$ -rays observed by HAWC makes the proton scenario for SS 433 unlikely, because the total energy required to produce the highly relativistic protons is too high. The jets of SS 433 are known to be radiatively inefficient, with most of the jet energy transformed into the thermal energy of W50<sup>16,27</sup> rather than into particle acceleration. We model the primary proton spectrum as a power law with an exponential cutoff,  $dN/dE_p \propto E_p^{-2} \exp(-E_p/1 \text{ PeV})$ . If we assume that 10% of the jet kinetic energy converts into accelerated protons, and that the ambient gas density<sup>16,27</sup> is  $0.05 \text{ cm}^{-3}$ , then the resulting flux of  $\gamma$ -rays from proton–proton collisions is much less than the observed  $\gamma$ -ray flux, as shown in the dash-dotted line of Fig. 2. In fact, for a target proton density as large as  $0.1 \text{ cm}^{-3}$  in the e1 region<sup>16,27</sup>, the total energy of the proton population needs to be around  $3 \times 10^{50} \text{ erg}$  to explain the observed  $\gamma$ -rays, assuming an  $E_\gamma^{-2}$  spectrum. This is comparable to the total jet energy available during the presumed 30,000-year lifetime<sup>2</sup> of SS 433. Furthermore, because the synchrotron emission from secondary electrons from charged pion decay is always lower than the  $\gamma$ -ray flux from  $\pi^0$  decay, and the observed X-ray flux is higher than the  $\gamma$ -ray flux, the X-rays cannot originate solely from secondary electrons. Finally, the proton scenario requires that the protons remain trapped in the region observed by HAWC for the lifetime<sup>2</sup> of SS 433. This means the protons must diffuse very slowly, with a diffusion coefficient of about 1/1,000 of the typical value<sup>28</sup> of the interstellar medium (ISM),  $D_{\text{ISM}} \approx 3 \times 10^{28} (E/3 \text{ GeV})^{1/3} \text{ cm}^2 \text{ s}^{-1}$ . This value, comparable to the theoretical Bohm limit, is very small but not impossible. Given the uncertainties in the historical jet flux, the ambient particle density and the radiative efficiency, we cannot exclude the possibility that some fraction of the  $\gamma$ -ray flux is produced by protons. However, we do rule out the possibility that the VHE  $\gamma$ -rays are entirely produced by protons.

Highly relativistic electrons, on the other hand, can produce  $\gamma$ -rays much more efficiently, primarily via inverse Compton scattering of CMB photons to  $\gamma$ -rays. The inverse Compton losses due to upscattering of infrared and optical photons are suppressed owing to the Klein–Nishina effect and are thus dominated by scattering of CMB photons<sup>29</sup>. In this scenario, the ratio of the VHE  $\gamma$ -ray to X-ray fluxes constrains the energy density in the magnetic field compared to the energy density in CMB photons. We have modelled the broadband spectral energy distribution of the eastern emission region 15' to 33' from the centre of SS 433. The solid and dashed lines in Fig. 2 show the spectral energy distribution of a leptonic model for e1 produced by an injected flux of relativistic electrons with an energy spectrum  $dN/dE \propto E^{-\alpha} \exp(-E/E_{\max})$  in a magnetic field of strength  $B$ . We use the parameters  $\alpha = 1.9$ ,  $E_{\max} = 3.5 \text{ PeV}$ , and  $B = 16 \mu\text{G}$  (see Methods). The estimate of the magnetic field strength is consistent with the

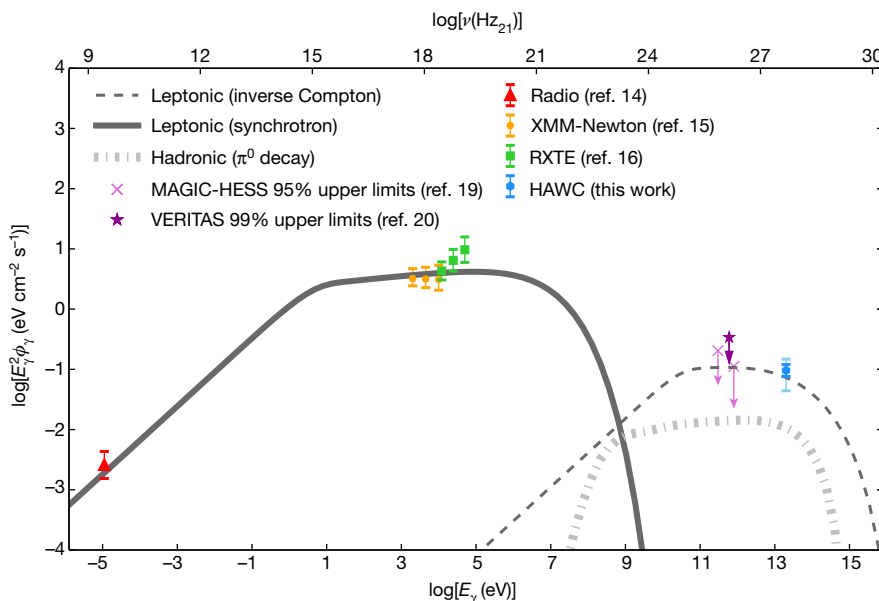


**Fig. 2 | Broadband spectral energy distribution of the eastern emission region e1.** The data include radio<sup>14</sup>, soft X-ray<sup>15</sup>, hard X-ray<sup>16</sup> and VHE  $\gamma$ -ray upper limits<sup>19,20</sup>, and HAWC observations of e1. Error bars indicate  $1\sigma$  uncertainties, with the thick (thin) errors on the HAWC flux indicating statistical (systematic) uncertainties and arrows indicating flux upper limits. The multiwavelength spectrum produced by electrons assumes a single electron population following a power-law spectrum

equipartition of energy between the relativistic electrons and magnetic fields, which is common in astrophysical systems<sup>16</sup>. The required total energy budget for relativistic electrons is three orders of magnitude lower than the total jet energy.

The maximum electron energy of about 1 PeV has important implications for electron acceleration sites and acceleration mechanisms in SS 433. SS 433 is distinguished from other binary systems with relativistic objects because it achieves a supercritical accretion of gas onto the central engine (the compact object)<sup>2</sup>. Powerful accretion flows and the inner jets near the compact object have therefore been proposed as possible acceleration sites of relativistic particles<sup>26</sup>. However, the observation from HAWC suggests that ultrarelativistic electrons are not accelerated near the centre of the binary. If the electrons were accelerated in the central region, they would have cooled by the time they reached the sites of observed VHE emission. Owing to their small gyroradii, high-energy electrons may transport in a magnetized medium via diffusion or advection. The distance travelled via diffusion within the cooling time  $t_{\text{cool}}$  of an electron of energy  $E$  moving in a magnetic field of strength  $B$  is  $r_d = 2\sqrt{Dt_{\text{cool}}} \approx 36 \text{ pc} (E/1 \text{ PeV})^{-1/3} (B/16 \mu\text{G})^{-1}$ , using the diffusion coefficient  $D$  typical of the ISM<sup>28</sup>. This distance would be even smaller for diffusion coefficients lower than the ISM value. Similarly, the distance travelled by electrons being advected with the jet flow is  $r_{\text{adv}} = 0.26c \times t_{\text{cool}} \approx 4 \text{ pc} (E/1 \text{ PeV})^{-1} (B/16 \mu\text{G})^{-2}$  for a jet velocity of  $0.26c$ . Both distance scales are smaller than the 40-pc distance between the binary and e1, indicating that the electrons are not accelerated near the centre of the system.

Instead, the highly energetic electrons in SS 433 are probably accelerated in the jets and near the VHE  $\gamma$ -ray emission regions. This presents a challenge to current acceleration models. For example, particle acceleration may be driven by the dissipation of the magnetic fields in the jets, but above several hundred teraelectronvolts the electron acceleration time exceeds the electron cooling time, assuming a  $16\text{-}\mu\text{G}$  magnetic field. Thus, the system does not appear to have sufficient acceleration power, unless there are very concentrated magnetic fields along the jets. If instead particle acceleration is driven by standing shocks produced by the bulk flow of the jets, it is possible to reach

with an exponential cutoff. The electrons produce radio to X-ray photons through synchrotron emission in a magnetic field (thick solid line) and teraelectronvolt  $\gamma$  rays through inverse Compton scattering of the CMB (thin dashed line). The dash-dotted line represents the radiation produced by protons, assuming that 10% of the jet kinetic energy converts into protons.

petaelectronvolt energies if the size of the acceleration region is larger than the gyroradii of the electrons. However, shocks in the interaction regions are not currently resolved by X-ray or  $\gamma$ -ray measurements.

Studies of microquasars such as SS 433 provide valuable probes of the particle acceleration mechanisms in jets, since these objects are believed to be scale models of the much larger and more powerful jets in active galactic nuclei<sup>30</sup>. Active galactic nuclei are the most prevalent VHE extragalactic sources and are believed to be the sources of the highest-energy cosmic rays. Although active galactic nuclei are not spatially resolved at VHE energies, with this observation we have identified a VHE source in which we can image the particle acceleration powered by jets. Future high-resolution observations of SS 433 are possible using atmospheric Cherenkov telescopes pointed to localize the emission sites better, and further high-energy measurements with HAWC will record the spectrum at high energies and better constrain the maximum energy of accelerated particles.

## Online content

Any methods, additional references, Nature Research reporting summaries, source data, statements of data availability and associated accession codes are available at <https://doi.org/10.1038/s41586-018-0565-5>.

Received: 24 May 2018; Accepted: 10 August 2018;

Published online 3 October 2018.

1. Margon, B. Observations of SS 433. *Annu. Rev. Astron. Astrophys.* **22**, 507–536 (1984).
2. Fabrika, S. The jets and supercritical accretion disk in SS433. *Astrophys. Space Phys. Rev.* **12**, 1–152 (2004).
3. Cherepashchuk, A. M. et al. INTEGRAL observations of SS433: results of coordinated campaign. *Astron. Astrophys.* **437**, 561–573 (2005).
4. Zealey, W. J., Dopita, M. A. & Malin, D. F. The interaction between the relativistic jets of SS433 and the interstellar medium. *Mon. Not. R. Astron. Soc.* **192**, 731–743 (1980).
5. Margon, B. & Anderson, S. F. Ten years of SS 433 kinematics. *Astrophys. J.* **347**, 448–454 (1989).
6. Safi-Harb, S. & Ögelman, H. ROSAT and ASCA observations of W50 associated with the peculiar source SS 433. *Astrophys. J.* **483**, 868–881 (1997).
7. Eikenberry, S. S. et al. Twenty years of timing SS 433. *Astrophys. J.* **561**, 1027 (2001).
8. Migliari, S., Fender, R. P. & Mendez, M. Iron emission lines from extended X-ray jets in SS 433: reheating of atomic nuclei. *Science* **297**, 1673 (2002).

9. Mirabel, I. & Rodríguez, L. F. Sources of relativistic jets in the galaxy. *Annu. Rev. Astron. Astrophys.* **37**, 409–443 (1999).
10. Begelman, M. C., King, A. R. & Pringle, J. E. The nature of SS433 and the ultraluminous X-ray sources. *Mon. Not. R. Astron. Soc.* **370**, 399–404 (2006).
11. Fabrika, S., Ueda, Y., Vinokurov, A., Sholukhova, O. & Shidatsu, M. Supercritical accretion discs in ultraluminous X-ray sources and SS 433. *Nat. Phys.* **11**, 551 (2015).
12. Cherepashchuk, A. M., Aslanov, A. A. & Kornilov, V. G. WBVR photometry of SS 433—spectra of the normal star and the accretion disk. *Sov. Astron.* **26**, 697–702 (1982).
13. Tetarenko, B. E., Sivakoff, G. R., Heinke, C. O. & Gladstone, J. C. WATCHDOG: a comprehensive all-sky database of galactic black hole X-ray binaries. *Astrophys. J. Suppl.* **222**, 15 (2016).
14. Geldzahler, B. J., Pauls, T. & Salter, C. J. Continuum observations of the supernova remnants W50 and G 74.9+1.2 at 2695 MHz. *Astron. Astrophys.* **84**, 237–244 (1980).
15. Brinkmann, W., Pratt, G. W., Rohr, S., Kawai, N. & Burwitz, V. XMM-Newton observations of the eastern jet of SS433. *Astron. Astrophys.* **463**, 611–619 (2007).
16. Safi-Harb, S. & Petre, R. Rossi X-ray timing explorer observations of the eastern lobe of W50 associated with SS 433. *Astrophys. J.* **512**, 784–792 (1999).
17. Aharonian, F. et al. TeV gamma-ray observations of SS-433 and a survey of the surrounding field with the HEGRA IACT-System. *Astron. Astrophys.* **439**, 635–643 (2005).
18. Hayashi, S. et al. Search for VHE gamma rays from SS433/W50 with the CANGAROO-II telescope. *Astropart. Phys.* **32**, 112–119 (2009).
19. Ahnen, M. L. et al. Constraints on particle acceleration in SS433/W50 from MAGIC and H.E.S.S. observations. *Astron. Astrophys.* **612**, A14 (2018).
20. Kar, P. VERITAS observations of high-mass X-ray binary SS 433. *Proc. Sci.* (35th Int. Cosmic Ray Conf.) ICRC2017, <https://doi.org/10.22323/1.301.0713> (2018).
21. Bordas, P., Yang, R., Kafexhiu, E. & Aharonian, F. Detection of persistent gamma-ray emission toward SS433/W50. *Astrophys. J.* **807**, L8 (2015).
22. Abeysekara, A. U. et al. The 2HWC HAWC Observatory Gamma Ray Catalog. *Astrophys. J.* **843**, 40 (2017).
23. López-Coto, R. et al. Effect of the diffusion parameters on the observed  $\gamma$ -ray spectrum of sources and their contribution to the local all-electron spectrum: the EDGE code. *Astropart. Phys.* **102**, 1–11 (2018).
24. Albert, J. et al. Variable very high energy gamma-ray emission from the microquasar LS I +61° 303. *Science* **312**, 1771–1773 (2006).
25. Archambault, S. et al. Exceptionally bright TeV flares from the binary LS I + 61° 303. *Astrophys. J.* **817**, L7 (2016).
26. Reynoso, M. M., Romero, G. E. & Christiansen, H. R. Production of gamma rays and neutrinos in the dark jets of the microquasar SS433. *Mon. Not. R. Astron. Soc.* **387**, 1745–1754 (2008).
27. Panferov, A. A. Jets of SS 433 on scales of dozens of parsecs. *Astron. Astrophys.* **599**, A77 (2017).
28. Ptuskin, V. S., Moskalenko, I. V., Jones, F. C., Strong, A. W. & Zirakashvili, V. N. Dissipation of magnetohydrodynamic waves on energetic particles: impact on interstellar turbulence and cosmic ray transport. *Astrophys. J.* **642**, 902–916 (2006).
29. Moderski, R., Sikora, M., Coppi, P. S. & Aharonian, F. A. Klein-Nishina effects in the spectra of non-thermal sources immersed in external radiation fields. *Mon. Not. R. Astron. Soc.* **364**, 1488 (2005).
30. Romero, G., Boettcher, M., Markoff, S. & Tavecchio, F. Relativistic jets in active galactic nuclei and microquasars. *Space Sci. Rev.* **207**, 5–61 (2017).

**Acknowledgements** We acknowledge support from: the US National Science Foundation (NSF); the US Department of Energy Office of High-Energy Physics; the Laboratory Directed Research and Development programme of Los Alamos National Laboratory; Consejo Nacional de Ciencia y Tecnología, México (grants 271051, 232656, 260378, 179588, 239762, 254964, 271737, 258865, 243290, 132197 and 281653) (Cátedras 873, 1563); Laboratorio Nacional HAWC de rayos gamma; L'OREAL Fellowship for Women in Science 2014; Red HAWC, México; DGAPA-UNAM (Dirección General Asuntos del Personal Académico—Universidad Nacional Autónoma de México; grants IG100317, IN111315, IN111716-3, IA102715, IN109916 and IA102917); VIEP-BUAP (Vicerrectoría de Investigación y Estudios de Posgrado-Benemérita Universidad Autónoma de Puebla); PIFI (Programa Integral de Fortalecimiento Institucional) 2012 and 2013; PRO-FOCIE (Programa de Fortalecimiento de la Calidad en Instituciones Educativas) 2014 and 2015; the University of Wisconsin Alumni Research Foundation; the Institute of Geophysics, Planetary Physics, and Signatures at Los Alamos National Laboratory; Polish Science Centre grant DEC-2014/13/B/ST9/945 and DEC-2017/27/B/ST9/02272; and Coordinación de la Investigación Científica de la Universidad Michoacana. We thank S. Delay, L. Díaz and E. Murrieta for technical support. We thank R. Mushotzky for providing the spectrum of the XMM-Newton data in the HAWC detection region.

**Reviewer information** *Nature* thanks A. Achterberg and M. Bowler for their contribution to the peer review of this work.

**Author contributions** C.D.R. and H. Zhou analysed the data and performed the maximum likelihood analysis. Multiwavelength modelling of the leptonic and hadronic emission was carried out by K.F. and H. Zhang, S.Y.B. and B.L.D. helped to prepare the manuscript. The entire HAWC Collaboration contributed through the construction, calibration and operation of the detector, the development and maintenance of reconstruction and analysis software, and the vetting of the analysis presented in this manuscript. All authors reviewed, discussed and commented on the results and the manuscript.

**Competing interests** The authors declare no competing interests.

#### Additional information

**Extended data** is available for this paper at <https://doi.org/10.1038/s41586-018-0565-5>.

**Reprints and permissions information** is available at <http://www.nature.com/reprints>.

**Correspondence and requests for materials** should be addressed to C.D.R. and H. Zhou.

**Publisher's note:** Springer Nature remains neutral with regard to jurisdictional claims in published maps and institutional affiliations.

## METHODS

**Data reduction and maximum likelihood analysis.** This analysis uses 1,017 days of data from the High Altitude Water Cherenkov (HAWC) Observatory collected between 26 November 2014 and 20 December 2017. The HAWC Observatory is an array of 300 tightly packed identical water Cherenkov detectors deployed 4,100 m above sea level on the slope of the volcano Sierra Negra, Mexico<sup>31</sup>. Each detector is a cylindrical water tank standing 5 m tall and 7.3 m in diameter, filled with 180,000 litres of purified water. At the bottom of each tank are four photomultipliers (PMTs) facing upward. The PMTs record the Cherenkov photons created by the relativistic secondary particles produced when primary cosmic rays and  $\gamma$ -rays interact at the top of the atmosphere. The HAWC array covers 22,000 m<sup>2</sup>. Its construction ended in December 2014, and the full array was commissioned in March 2015.

Using the relative arrival time of photoelectrons (hits) detected by the PMTs, the arrival direction of primary  $\gamma$ -rays can be reconstructed with an accuracy<sup>32</sup> of around 1° below 1 TeV to <0.2° above 10 TeV. The accuracy of the reconstruction determines the point spread function of the detector, and is a function of the energy, zenith angle and composition of the primary particle. Air showers from  $\gamma$ -rays are discriminated from the nearly isotropic background of hadronic cosmic rays by filtering out ‘clumpy’ patterns of hits, which are characteristic of the energy deposited in hadronic air showers. The cosmic-ray background rejection efficiency improves rapidly as a function of energy<sup>32</sup>, increasing from 90% at 1 TeV to 99.9% at 10 TeV.

To compute the statistical significance of  $\gamma$ -ray emission observed with HAWC, a maximum likelihood fit using parametric spatial and spectral models is applied to the data<sup>33,34</sup>. The models are forward-folded through the detector response to produce expected counts of  $\gamma$ -ray signal events and cosmic-ray background events. The expectation is then compared to the observed counts  $N_{\text{obs}}$ . To calculate the expected counts as a function of position on the sky, the events are binned in a fine mesh using the HEALPix pixelization of the unit sphere<sup>35</sup>. The pixelization is chosen to be 0.1°, roughly two to five times smaller than the radius of the instrument point spread function. To apply models of the energy spectrum of a source, the data are binned according to the fraction of PMTs in the detector triggered by an air shower<sup>32</sup>. This measure of shower ‘size’ is used as a coarse proxy for the energy of the primary particle; a total of nine size bins labelled  $B = 1–9$  is used.

Given a model  $\theta$  with spatial and spectral parameters, we maximize the likelihood of the model having produced the data as follows:

$$\ln \mathcal{L}(N_{\text{obs}}|\theta) = \sum_{B=1}^9 \sum_{j=1}^m \ln P(N_{\text{obs}}^{j,B}|\theta)$$

where the sum runs over the size bins  $B$  and the HEALPix pixels  $j$  in the region of interest (ROI) of the fit.  $P$  is the Poisson probability of detecting  $N_{\text{obs}}^{j,B}$  events in pixel  $j$  and size bin  $B$  given the model parameters  $\theta$ .

Within the ROI around SS 433 defined in Extended Data Fig. 1, two fits are performed to maximize the likelihood: a fit which accounts only for the emission from MGRO J1908+06 (null hypothesis), and a fit that accounts for the combined emission from MGRO J1908+06 and the SS 433 region (alternative hypothesis). The ratio of the maximum likelihood defines a test statistic (TS):

$$\text{TS} = 2(\ln \mathcal{L}(N_{\text{obs}}|\theta_{\text{alt}}) - \ln \mathcal{L}(N_{\text{obs}}|\theta_0))$$

where  $\theta_0$  and  $\theta_{\text{alt}}$  represent the spatial and spectral parameters of the null and alternative hypotheses, respectively. TS is then converted to a  $P$  value to estimate the statistical significance of emission from SS 433. As discussed in the main text, the alternative hypothesis assumes two point sources with power-law spectra  $dN/dE = f_0(E/20 \text{ TeV})^{-2}$ , where the flux normalization  $f_0$  is the free parameter of the spectral model.

Wilks’ Theorem is used to convert TS to a  $P$  value<sup>36</sup>. In the joint likelihood maximization, there are two degrees of freedom (d.o.f.) for the two separately fitted flux normalizations of the hotspots at w1 and e1. Therefore, we calculate the one-tailed  $P$  value  $\text{pr}(\text{TS} > \chi^2 = 41.2 | \text{d.o.f.} = 2) = 1.13 \times 10^{-9}$ . This is the tail probability of  $\text{TS} > 41.2$  assuming that, under the null hypothesis of no excess  $\gamma$  rays, TS follows a  $\chi^2$  distribution with 2 degrees of freedom. Since the positions of the point source fits at w1 and e1 were chosen after looking into the data, and because we are searching for other microquasars in the field of view of HAWC, we must apply a posteriori corrections to the  $P$  value to account for multiple-comparison effects.

The X-ray interaction regions w1, w2, e1, e2 and e3 are a priori candidates for the locations of the maxima, as is the centre of the binary system, for a total of six potential hotspots. Given the angular resolution of HAWC, it would not be possible to spatially resolve all six hotspots; at best three regions (east, west and centre) can be separately fitted with confidence. There are 23 possible combinations of the six a priori locations that can be used to fit one, two or three hotspots in the eastern, central and western regions of the source. We add an additional 12 trials

to account for the known microquasars in the field of view of HAWC<sup>9,13,37</sup>. This trial factor is conservative given that several Galactic microquasars are already known teraelectronvolt sources<sup>38,39</sup>. Given 35 total trials, the corrected  $P$  value is  $3.96 \times 10^{-8}$ , which corresponds to a statistical significance of 5.4 $\sigma$ .

**Modelling of the nearby extended source MGRO J1908+06.** A bright extended source, MGRO J1908+06, is detected with more than  $30\sigma$  in this dataset and is located less than 2° from the  $\gamma$ -ray hotspots of SS 433 (Extended Data Fig. 1). The region of MGRO J1908+06 contains a pulsar and a supernova remnant, but it is not clear whether the observed teraelectronvolt  $\gamma$ -ray emission is from either or both of them. A detailed discussion of MGRO J1908+06 is beyond the scope of this paper. However, the morphology of MGRO J1908+06 must be carefully studied to minimize the contamination of the emission due to MGRO J1908+06 on the fluxes of the lobes.

A maximum likelihood analysis is performed that simultaneously fits the emission from MGRO J1908+06 and the hotspots at w1 and e1. An electron diffusion model appropriate for older pulsar wind nebulae<sup>23,40</sup> is used to describe the spatial morphology of MGRO J1908+06. Given the uncertainty of the nature of MGRO J1908+06, two other spatial models with Gaussian and power law radial profiles are also tested in the simultaneous fit. The choice of spatial model affects the best-fit fluxes from e1 and w1 at the level of  $\pm 20\%$ . We adopt this value as a systematic uncertainty on the flux from w1 and e1 due to VHE emission from the nearby extended source.

**Contamination from galactic diffuse emission.** The e1 and w1 regions are located roughly 2° from the Galactic plane, so the contamination from the Galactic diffuse emission (GDE) is negligible. However, MGRO J1908+06 has a Galactic latitude of about 1°. Since the three spatial models used to fit MGRO J1908+06 are radially symmetric, the presence of GDE has the potential to produce an overestimate in the flux from MGRO J1908+06, which could result in an underestimate in the flux measured from w1 and e1. To minimize the effect of the GDE on the fit, the ROI is defined to be a semicircular region centred on the position of MGRO J1908+06 (Extended Data Fig. 1). The ROI is designed to reduce the effect of GDE by excluding the half of the source closest to the Galactic plane.

To estimate the systematic uncertainties associated with the choice of ROI and possible contamination from GDE, a second maximum likelihood fit is performed using a full-disk ROI that includes GDE, emission from MGRO J1908+06, and w1 and e1. The spatial distribution of the GDE is modelled with a Gaussian profile of three different widths of 0.5°, 1° and 2° in Galactic latitude, and is treated as constant in Galactic longitude over the width of the ROI. Comparing the results to the fit with a semicircular ROI indicates that contamination from GDE is less than 10% for e1 and less than 20% for w1.

**Fit results.** The fit results are reported in Extended Data Table 1. Fitting the emission from w1 and e1 simultaneously, we calculate  $\text{TS} = 41.2$ , which corresponds to a  $5.4\sigma$  observation ( $P = 3.96 \times 10^{-8}$ ) after accounting for a posteriori statistical trial factors. To check the consistency of the results, we also fit w1 and e1 separately, redefining the alternative model to include MGRO J1908+06 and only e1 or w1. The significance of the VHE excess from these locations is below  $5\sigma$  in the fits, but the estimated fluxes are consistent with the simultaneous fit.

An additional check is made on the effect of fixing versus floating the best-fit positions of the emission from the east and west hotspots. In the original alternative hypothesis, the point sources are centred on e1 and w1. Here, the positions of the point sources are made additional free parameters in the point source fit. We find that allowing the positions of the teraelectronvolt hotspots to vary does not affect the flux estimates, which are consistent with the fixed-position fits. Moreover, the best-fit positions of the east and west teraelectronvolt emission regions are consistent with e1 and w1 within statistical uncertainties.

The choice of spectral model also affects the estimated  $\gamma$ -ray flux at 20 TeV. Extended Data Table 2 shows the dependence of the best-fit VHE flux from e1 and w1 on the assumed spectral models, including statistical uncertainties on the flux normalization at 20 TeV. Two spectral models were tested: a simple power law  $dN/dE_\gamma \propto E_\gamma^{-\alpha}$ , and a power law with an exponential cutoff  $dN/dE_\gamma \propto E_\gamma^{-\alpha} \exp(-E_\gamma/E_{\text{cut}})$ . The choice of spectral model can alter the flux normalization by almost a factor of two compared to the default  $E^{-2}$  model.

**Summary of systematic uncertainties.** The systematic uncertainties in the estimated fluxes from the teraelectronvolt hotspots of SS 433 include the following contributions: detector systematic effects, modelling ambiguities in MGRO J1908+06, and contamination from Galactic diffuse emission. The systematic uncertainties due to the modelling of MGRO J1908+06 and the contamination from Galactic diffuse emission are  $\pm 20\%$  and  $-10\%$  ( $-20\%$ ) for the east (west) hotspot, respectively, and are discussed in previous sections.

The detector response is estimated using Monte Carlo simulations and then optimized using observations of the Crab Nebula<sup>32</sup>, which appears point-like in the HAWC data. Systematic uncertainties that potentially affect the result presented here include the charge resolution and relative quantum efficiency of the PMTs, the absolute quantum efficiency of the PMTs, changes to the detector layout as

construction proceeded, uncertainties in the point spread function, and systematic differences in the distribution of arrival times of photoelectrons between data and simulation. The total systematic uncertainty on the flux normalization from detector effects is  $\pm 50\%$ .

All the components of the systematic uncertainties are summarized in Extended Data Table 3 and combined in quadrature to estimate the total systematic uncertainty on the VHE flux from w1 and e1. We note that since the systematic uncertainties due to MGRO J1908+06 and GDE are anti-correlated, the quadrature sum overestimates the total systematic uncertainty. However, the effect is not particularly important, since the detector systematic effects are the dominant source of uncertainty.

**X-ray template fit and upper limit on the extent of the emission regions.** We performed several maximum likelihood fits modelling the hotspots as spatially extended sources. In the first fit, we generated spatial templates for the eastern and western regions based on the X-ray contours published by ROSAT<sup>41</sup> and then performed a joint likelihood fit with the two  $\gamma$ -ray hotspots and MGRO J1908+06. This produces no improvement in TS over a point-source fit.

To constrain the size of the  $\gamma$ -ray emission regions, likelihood fits are applied using a Gaussian morphology convolved with the point spread function of HAWC. To reduce the number of free parameters, we first fitted MGRO J1908+06 using an ROI with SS 433 and its hotspots excluded. The extended fit from MGRO J1908+06 is then subtracted from the data, and the residual  $\gamma$ -ray emission from the  $\gamma$ -ray hotspots is fitted using two Gaussian functions. The centres of the Gaussians are fixed to e1 and w1, and their angular widths are estimated in a simultaneous fit to both the eastern and western regions.

The maximum likelihood fit yields an angular width of  $0.14 \pm 0.06$  degrees for the east hotspot and  $0.08^{+0.14}_{-0.05}$  degrees for the west hotspot. We estimate the 90% confidence region on the extent as the value of Gaussian width that produces a decrease  $\Delta TS = -2.71$  from the maximum likelihood value. The resulting 90% upper limits are  $0.25^\circ$  for the east region and  $0.35^\circ$  for the west region.

**Upper limit on emission from the central binary.** In the present dataset, no statistically significant emission is observed from the centre of SS 433. Using Feldman-Cousins likelihood ordering<sup>42</sup>, we estimate the 90% upper limit on the flux at 20 TeV to be  $5.3 \times 10^{-17}$  TeV $^{-1}$  cm $^{-2}$  s $^{-1}$  after fitting MGRO J1908+06 and the emission at e1 and w1.

**Upper limit on detected  $\gamma$ -ray energy.** The binning of  $\gamma$ -ray events into size bins  $B$  causes us to lose information about the energies of the  $\gamma$  rays observed from SS 433. To determine the upper energy bound on the flux we observe, we scan over the maximum energy  $E_{\gamma,\max}$  used in the forward-folding analysis. Starting at  $E_{\gamma,\max} = 15$  TeV, we find that TS increases monotonically until  $E_{\gamma,\max} = 25$  TeV. Increasing  $E_{\gamma,\max}$  above this value causes TS to plateau (for e1) or decrease slightly (w1). We infer that the current measurement of e1 and w1 implies a minimum  $E_{\gamma,\max} = 25$  TeV, and report this as a conservative estimate of the highest energy observed by HAWC.

**Study of residual emission in the region of interest.** As a final check of the quality of the maximum likelihood fits, we plot the distribution of the significance values in each HEALPix pixel in the ROI around SS 433 in Extended Data Fig. 2. The significance values are plotted in units of Gaussian  $\sigma$ . If only random background fluctuations are present, the significance values follow a standard normal distribution, shown by the dashed line in the figure.

Prior to the maximum likelihood fit, the significance distribution in the ROI is considerably skewed towards positive values owing to excess counts above background from MGRO J1908+06 and  $\gamma$ -rays from w1 and e1 (left panel of Extended Data Fig. 2). After the subtraction of the maximum likelihood fit to emission from MGRO J1908+06 (middle panel), the skew in the distribution is considerably reduced, though still visible owing to excess counts from the interaction regions near SS 433. Finally, subtraction of the maximum likelihood flux from w1 and e1 produces a distribution that, within statistical uncertainties, is equivalent to background fluctuations (right panel of Extended Data Fig. 2).

**Multiwavelength modelling of the spectral energy distribution.** To determine the origin of the VHE radiation, we model the broadband emission from e1 using 2.7 GHz radio measurements from the Effelsberg Telescope<sup>14</sup>, soft X-ray measurements between 2 keV and 10 keV from XMM-Newton<sup>15</sup>, hard X-ray measurements between 10 keV and 50 keV from the Rossi X-ray Timing Explorer<sup>16</sup>, VHE  $\gamma$ -ray upper limits from the MAGIC, H.E.S.S. and VERITAS imaging air Cherenkov telescopes<sup>19,20</sup>, and HAWC observations. The data are taken from the region  $15'$  to  $33'$  east of SS 433, which covers the excess observed by HAWC centred at e1. Leptonic and hadronic models are used to produce spectral energy distributions for the low- and high-energy emission. The spectral energy distributions are shown in Fig. 2, and discussion of the two models is provided below.

**VHE emission due to leptonic interactions.** In the leptonic scenario considered in this paper, relativistic electrons scatter photons from the CMB photons to TeV energies via the inverse Compton process, and produce X-ray and radio emissions

by the synchrotron radiation. Although a far-infrared background in the lobe may contribute to the production of sub-TeV photons, no appreciable infrared emission has been reported near the  $\gamma$ -ray emission region<sup>2,43</sup>. The electron spectrum is obtained by solving the continuity equation, considering radiative cooling<sup>44</sup>. The best-fit values of the parameters of the injection spectrum, including the flux, spectral index and maximum energy of the electrons, and the magnetic field strength in the source region, are obtained through Markov Chain Monte Carlo<sup>45</sup> sampling of their likelihood distributions when fitting to the multiwavelength data. The radio and soft X-ray data points correspond to the Effelsberg Telescope<sup>14</sup> and the XMM-Newton (the Mos1 detector)<sup>15</sup> observations of a  $6'$  circle centred on e1. A 30% uncertainty attributed to the unknown shape of the HAWC source is added to the statistical and systematic errors of the observational data, though we find that the uncertainty has a negligible impact on the fit. The hard X-ray data points and the sub-teraelectronvolt upper limits are set by the RXTE, MAGIC, H.E.S.S., and VERITAS observations of the e1 region<sup>16,19,20</sup>.

The VHE flux is determined using the flux from e1 at 20 TeV reported in Extended Data Table 1, where separate fits were made to eastern and western hotspots, and the positions were fixed to e1 and w1. The best-fit values of the injection spectrum and magnetic field in the emission region are  $\alpha = 1.87^{+0.04}_{-0.07}$ ,  $\log[E_{\max}(\text{PeV})] = 3.53^{+0.31}_{-0.38}$  and field strength  $B = 16.04^{+5.60}_{-2.23}\mu\text{G}$ . Taking the distance to the source to be 5.5 kpc, the fit suggests a total electron energy of  $2.9 \times 10^{47}$  erg. This is a small fraction of the total energy deposited by the jets of SS 433 over their lifetime, which is about  $9 \times 10^{50}$  erg assuming a kinetic jet luminosity<sup>2</sup> of  $10^{39}$  erg s $^{-1}$ . Future multiwavelength observations dedicated to the VHE  $\gamma$ -ray emission region will better constrain the magnetic field strength and the properties of the electron population.

We note that the presence of several hundred teraelectronvolt-to-petaelectron-volt electrons would challenge the current particle acceleration mechanisms. Successful acceleration requires that the acceleration rate  $\dot{\gamma} \approx eBv/m_ec^2$ , where  $e$  is the charge of the electron and  $m_e$  is the electron mass, based on heuristic considerations (where  $v$  is the velocity associated with the notional electromotive force) exceed the cooling rate  $\dot{\gamma} \approx 4c\sigma_T\gamma^2(B^2/8\pi)/3m_ec^2$ , assuming that synchrotron radiation dominates the cooling processes in the lobes of SS 433. This leads to a maximum electron energy  $E_{e,\max} = 271$  TeV ( $v/100$  km s $^{-1}$ ) $^{1/2}$  ( $B/16\mu\text{G}$ ) $^{-1/2}$ . For reference, the Alfvén speed in the lobes is  $v_A = 160$  km s $^{-1}$  ( $n_b/0.05$  cm $^{-3}$ ) $^{-1/2}$  ( $B/16\mu\text{G}$ ). A higher Alfvén speed could be achieved if the acceleration takes place in the central spine of the jet, where the mass loading due to black hole accretion is smaller and the magnetic field is stronger. Depending on the exact electron acceleration mechanisms,  $v$  could be associated with the jet flow velocity, or with the Alfvén speed. In both cases, using these estimates, it is possible that the maximum electron energy could exceed 1 PeV. However, the timescale of acceleration mechanisms such as second-order Fermi acceleration is proportional to  $(v/c)^2$ , making the production of several hundred teraelectron-volt electrons less efficient. Future VHE  $\gamma$ -ray and hard X-ray observations can better constrain the electron cutoff energy, and diagnose the in situ particle acceleration mechanism.

**VHE emission due to hadronic interactions.** In the hadronic scenario, high-energy protons interact with the ambient gas in the source, and produce  $\gamma$  rays via the decay  $\pi^0 \rightarrow \gamma\gamma$ . Extended Data Fig. 3 shows the fraction of jet power that needs to be converted to protons to produce the observed  $\gamma$ -ray flux. We assume a proton spectrum  $dN/dE_p \propto E_p^{-\alpha} \exp(-E_p/E_{\max})$ , and adopt a proton–proton interaction cross-section<sup>46</sup> of around 50 mb, and a baryon density<sup>16,27</sup> of  $0.01\text{--}0.1$  cm $^{-3}$ . The total proton energy is obtained by integrating this spectrum normalized to the VHE  $\gamma$ -ray flux.

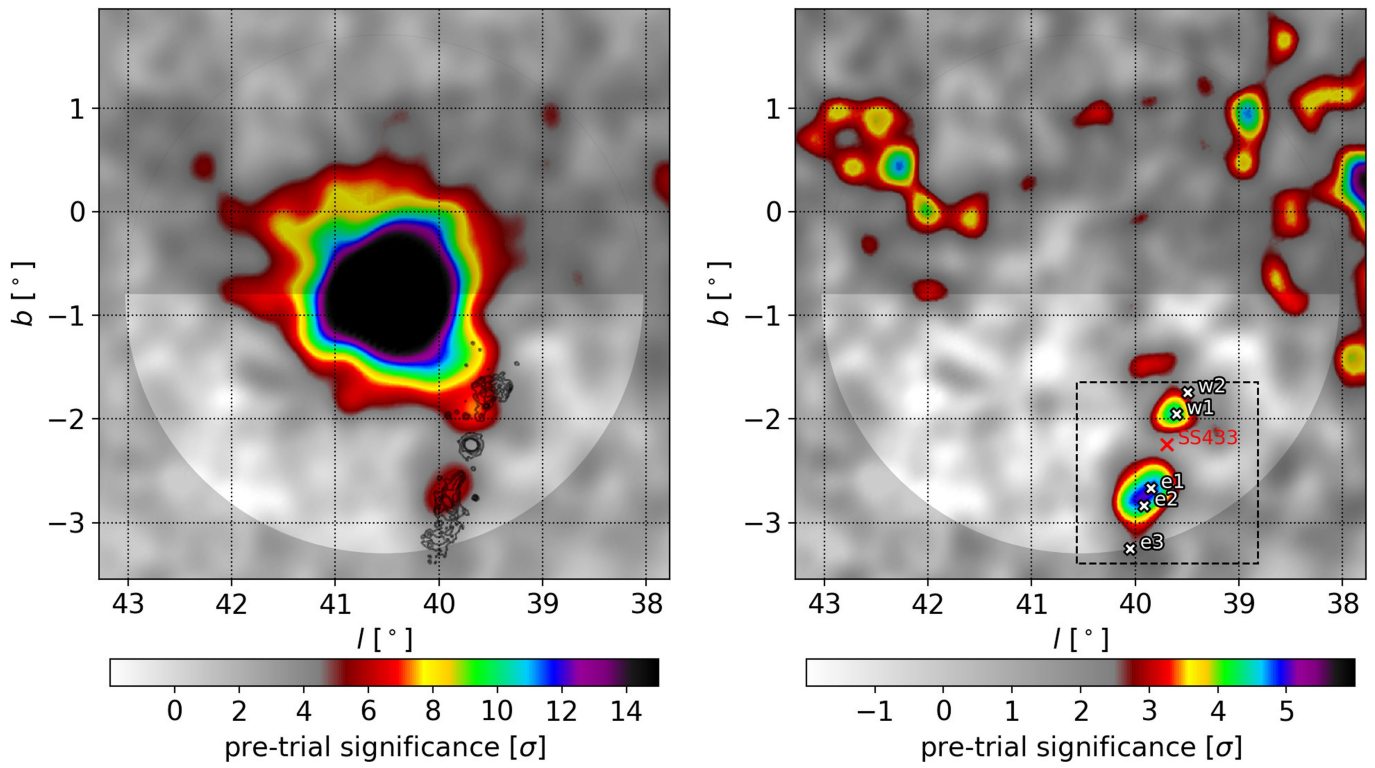
If the diffusion coefficient in the source is comparable to that in the ISM, no hadronic models would be allowed, because they would require a proton injection rate that exceeds the total kinetic luminosity of the jets of SS 433. Even in extreme circumstances, for example, where the diffusion coefficient is extremely small, possibly owing to scattering by turbulence generated from the streaming cosmic rays<sup>47,48</sup>, particles could remain in the jet as long as the jet lifetime<sup>2</sup> of around  $10^4$  years. Assuming that protons follow a hard spectrum with  $\alpha < 2$ , the hadronic scenario would still require that at least 30% of the jet power goes to protons. Although a hadronic origin to the VHE flux is possible, it requires rather extreme source parameters and is therefore disfavoured.

**Code availability.** The study was carried out using the Analysis and Event Reconstruction Integrated Likelihood Fitting Framework (AERIE-LiFF) developed by the HAWC Collaboration. The software is open-source and publicly available on Github: <https://github.com/rjlauer/aerie-liff>. The code distribution includes instructions on installation and usage.

## Data availability

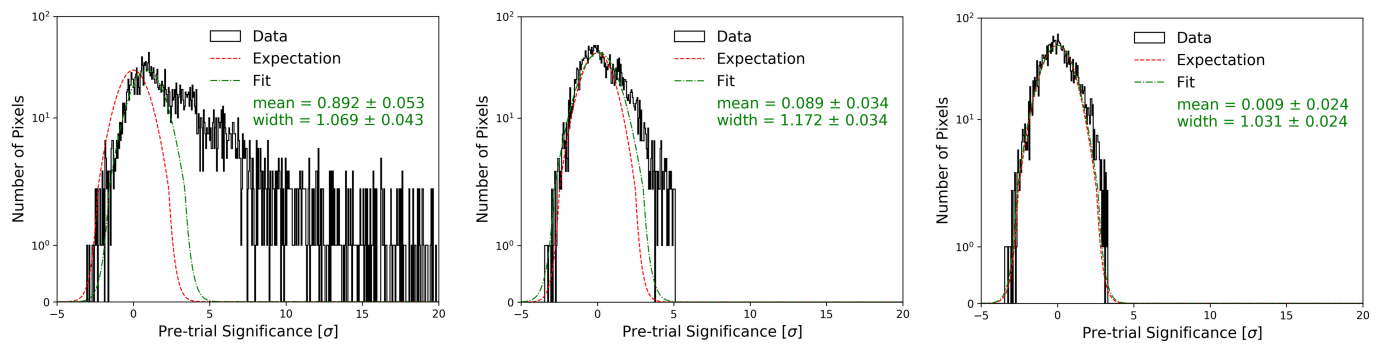
The datasets analysed during this study are available at a public repository maintained by the HAWC Collaboration: <https://data.hawc-observatory.org/>.

31. Smith, A. J. HAWC: design, operation, reconstruction and analysis. *Proc. Sci.* (34th Int. Cosmic Ray Conf.) ICRC2015, <https://doi.org/10.22323/1.236.0966> (2016).
32. Abeysekara, A. U. et al. Observation of the Crab Nebula with the HAWC Gamma Ray Observatory. *Astrophys. J.* **843**, 39 (2017).
33. Younk, P. W. et al. A high-level analysis framework for HAWC. *Proc. Sci.* (34th Int. Cosmic Ray Conf.) ICRC2015, <https://doi.org/10.22323/1.236.0948> (2016).
34. Vianello, G. et al. The multi-mission maximum likelihood framework. *Proc. Sci.* (34th Int. Cosmic Ray Conf.) ICRC2015, <https://doi.org/10.22323/1.236.1042> (2016).
35. Gorski, K. M. et al. HEALPix—a framework for high resolution discretization, and fast analysis of data distributed on the sphere. *Astrophys. J.* **622**, 759–771 (2005).
36. Wilks, S. S. The large-sample distribution of the likelihood ratio for testing composite hypotheses. *Ann. Math. Stat.* **9**, 60–62 (1938).
37. Chaty, S. & Delautier, S. Microquasars. <http://www.aim.univ-paris7.fr/CHATY/Microquasars/microquasars.html> (Université Paris Diderot, 2006).
38. Aharonian, F. et al. Discovery of very high energy gamma rays associated with an X-ray binary. *Science* **309**, 746–749 (2005).
39. Aliu, E. et al. Multiwavelength observations of the TeV binary LS I +61 303 with VERITAS, Fermi-LAT, and Swift/XRT during a TeV outburst. *Astrophys. J.* **779**, 88 (2013).
40. Abeysekara, A. U. et al. Extended gamma-ray sources around pulsars constrain the origin of the positron flux at Earth. *Science* **358**, 911–914 (2017).
41. Brinkmann, W., Aschenbach, B. & Kawai, N. ROSAT observations of the W 50/SS 433 system. *Astron. Astrophys.* **312**, 306–316 (1996).
42. Feldman, G. J. & Cousins, R. D. A unified approach to the classical statistical analysis of small signals. *Phys. Rev. D* **57**, 3873–3889 (1998).
43. Fuchs, Y., Mirabel, I. F. & Ogley, R. N. Mid-infrared observations of GRS 1915+105 and SS 433. *Astrophys. Space Sci. Suppl.* **276**, 99–100 (2001).
44. Finke, J. D. & Dermer, C. D. Cosmic ray electron evolution in the supernova remnant RX J1713.7-3946. *Astrophys. J.* **751**, 65 (2012).
45. Foreman-Mackey, D., Hogg, D. W., Lang, D. & Goodman, J. emcee: the MCMC hammer. *Publ. Astron. Soc. Pacif.* **125**, 306–312 (2013).
46. Particle Data Group. Review of particle physics. *Phys. Lett. B* **592**, 1–5 (2004).
47. Amato, E. & Blasi, P. Non linear particle acceleration at non-relativistic shock waves in the presence of self-generated turbulence. *Mon. Not. R. Astron. Soc.* **371**, 1251–1258 (2006).
48. Malkov, M. A., Diamond, P. H., Sagdeev, R. Z., Aharonian, F. A. & Moskalenko, I. V. Analytic solution for self-regulated collective escape of cosmic rays from their acceleration sites. *Astrophys. J.* **768**, 73 (2013).



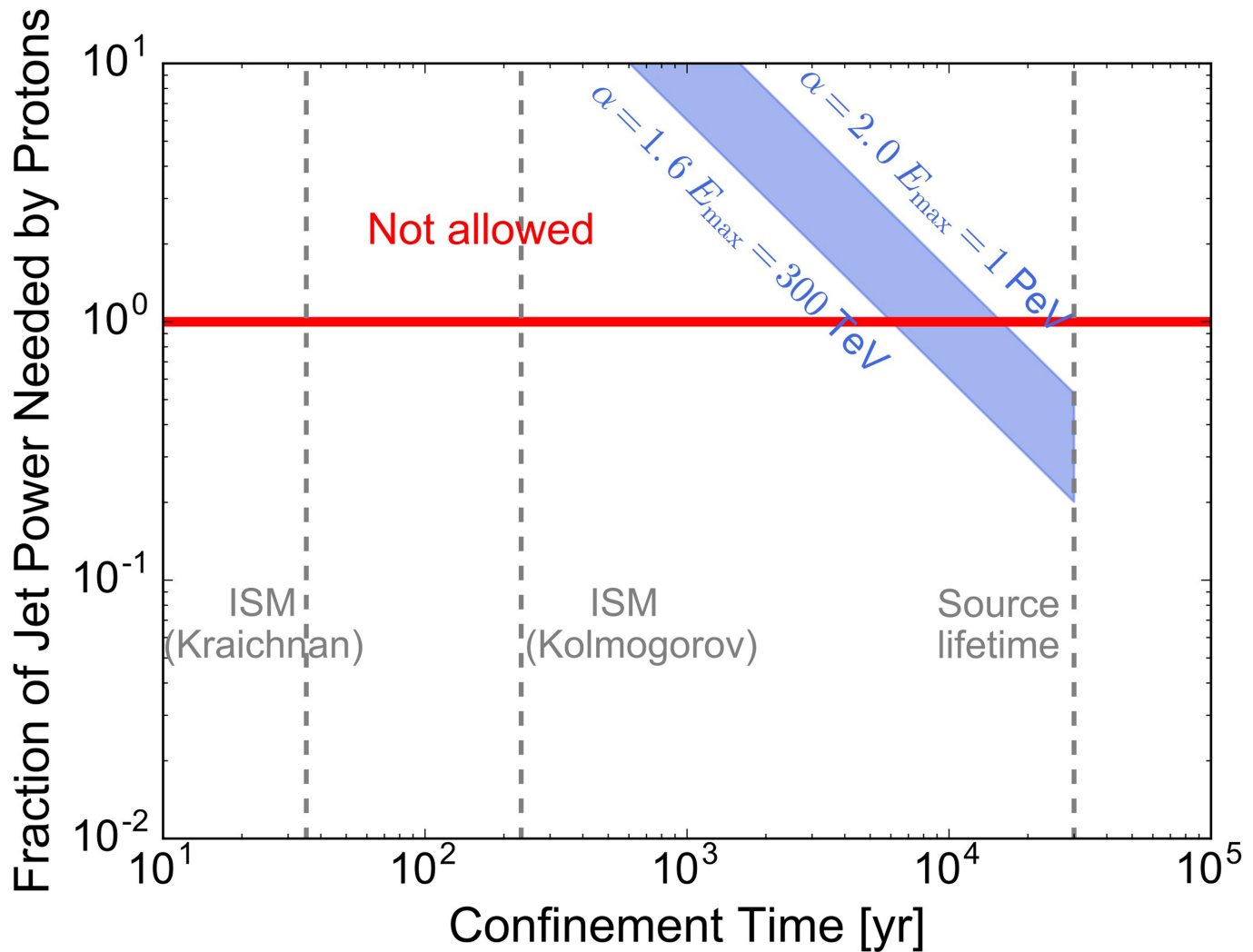
**Extended Data Fig. 1 | VHE  $\gamma$  rays from MGRO J1908+06 and SS 433/W50.** The colour scale indicates the statistical significance of the excess counts above the background of contaminating cosmic rays and  $\gamma$ -rays before accounting for statistical trials. The bright extended  $\gamma$ -ray source MGRO J1908+06 is shown at the centre of the left panel with SS 433/W50 at the bottom. The dark contours show X-ray emission from SS 433 and its

jets<sup>41</sup>. The semicircular area indicates the region of interest used to fit the  $\gamma$ -ray observations. The right panel shows the  $\gamma$ -ray excess measured after the fitting and subtraction of  $\gamma$ -rays from the spatially extended source MGRO J1908+06. The dashed box indicates the region shown in Fig. 1. The jet termination regions  $e_1$ ,  $e_2$ ,  $e_3$ ,  $w_1$  and  $w_2$  observed in the X-ray data are indicated, as well as the location of the central binary.



**Extended Data Fig. 2 | Distribution of pixel significance in the region of interest of the fit.** The significance is defined as deviations from the background expectation, in the HAWC sky map (left panel), after fitting

and subtraction of emission from MGRO J1908+06 (middle panel), and after fitting and removal of emission from MGRO J1908+06 and the  $\gamma$  rays from w1 and e1 (right panel).



**Extended Data Fig. 3 | Fraction of jet power needed to produce the observed VHE  $\gamma$ -rays in the hadronic scenario.** The blue-shaded region shows the energy injection rate of protons, in units of the kinetic luminosity of the jet, required to produce the observed VHE  $\gamma$ -rays by interacting with ambient gas, as a function of the proton confinement time. A gas density of  $0.05 \text{ cm}^{-3}$  is adopted for the source vicinity<sup>16,27</sup>. Most hadronic models require  $>100\%$  jet power (above the red solid line)

and are thus not allowed. Even when the diffusion coefficient is extremely small (for reference, the dashed grey lines show the source age and the confinement time of 200 TeV protons in a 30-pc region in the ISM with Kraichnan- and Kolmogorov-type diffusion) and when the spectral index is much harder than 2, the hadronic scenario still requires a large energy input from the jet.

Extended Data Table 1 | Fits to teraelectronvolt emission from SS 433 using nested point source models

Lobe	Position (RA, Dec)	$dN/dE$ at 20 TeV [ $10^{-16}$ TeV $^{-1}$ cm $^{-2}$ s $^{-1}$ ]	TS	Significance (post-trials)
<b>Simultaneous fit to E+W hotspots, positions fixed.</b>				
E	19:13:37 04°55'48"	$2.4^{+0.6+1.3}_{-0.5+1.3}$	41.2	$5.4\sigma$
W	19:10:37 05°02'13"	$2.1^{+0.6+1.2}_{-0.5-1.2}$		
<b>Separate fit to E+W hotspots, positions fixed.</b>				
E	19:13:37 04°55'48"	$2.5^{+0.7+1.4}_{-0.5-1.4}$	24.3	$4.6\sigma$
W	19:10:37 05°02'13"	$2.3^{+0.7+1.3}_{-0.5-1.3}$	20.4	$4.2\sigma$
<b>Separate fit to E+W hotspots, positions floated.</b>				
E	19:14:11 $^{+20s}_{-39s}$ 04°59'10" $^{+03/30"}_{-06/18"}$	$2.6^{+0.6+1.4}_{-0.5-1.4}$	26.9	$4.4\sigma$
W	19:10:40 $^{+17s}_{-17s}$ 05°03'40" $^{+03/32"}_{-04/55"}$	$2.4^{+0.6+1.3}_{-0.5-1.3}$	23.4	$4.0\sigma$

$dN/dE$  is the  $\gamma$ -ray flux, RA, right ascension; Dec., declination. TS, test statistic.

**Extended Data Table 2 | Dependence of measured HAWC flux at 20 TeV on spectral assumption, assuming a power law in energy parameterized by a spectral index and an exponential cutoff parameterized by  $E_{\text{cutoff}}$**

$E_{\text{cutoff}}$	$dN/dE$ at 20 TeV [ $\times 10^{-16}$ TeV $^{-1}$ cm $^{-2}$ s $^{-1}$ ]						
	Index: -1.5		Index: -2.0		Index: -2.5		West Lobe
	East Lobe	West Lobe	East Lobe	West Lobe	East Lobe	West Lobe	
No cutoff	$1.0^{+0.3}_{-0.2}$	$0.9^{+0.3}_{-0.2}$	$2.4^{+0.6}_{-0.5}$	$2.1^{+0.6}_{-0.5}$	$3.3^{+0.9}_{-0.7}$	$2.4^{+0.9}_{-0.6}$	
50 TeV	$4.7^{+1.1}_{-0.9}$	$4.2^{+1.1}_{-0.9}$	$5.0^{+1.2}_{-1.0}$	$4.1^{+1.3}_{-0.9}$	$3.2^{+0.9}_{-0.7}$	$1.7^{+1.1}_{-0.7}$	
300 TeV	$1.7^{+0.5}_{-0.4}$	$1.6^{+0.5}_{-0.4}$	$3.3^{+0.8}_{-0.7}$	$2.9^{+0.8}_{-0.7}$	$3.6^{+0.9}_{-0.7}$	$2.4^{+0.9}_{-0.7}$	

**Extended Data Table 3 | Systematic uncertainties on the flux of VHE  $\gamma$ -rays from SS 433 measured by HAWC**

Systematic	East Lobe	West Lobe
Detector Systematic Effects		$\pm 50\%$
MGRO J1908+06 Modeling		$< \pm 20\%$
Galactic Diffuse Contamination	-10%	-20%
Total	$\pm 55\%$	$\pm 55\%$